Original Article

Powder-metallurgy fabrication of ZrB_2–hardened Zr_3Al_2 intermetallic composites by high-energy ball-milling and reactive spark-plasma sintering

Jesús López-Arenal [a], Bibi Malmal Moshtaghioun [a,*],
Francisco L. Cumbrera [a], Diego Gómez-García [a], Angel L. Ortiz [b,**]

[a] Departamento de Física de la Materia Condensada, Universidad de Sevilla, 41080, Sevilla, Spain
[b] Departamento de Ingeniería Mecánica, Energética y de los Materiales, Universidad de Extremadura, 06006, Badajoz, Spain

ARTICLE INFO

ABSTRACT

A powder metallurgy route combining high-energy ball-milling (HEBM) of elemental powders and reactive spark-plasma sintering (SPS) is proposed for the controlled fabrication of novel composites based on a Zr–Al intermetallic matrix hardened with a ceramic second-phase. As proof-of-concept, its suitability is demonstrated on ZrB_2–hardened Zr_3Al_2. Specifically, commercially available powders of ZrH_2, Al, and B were first combined in molar ratios of 2:1:1 to give an intermetallic–ceramic composite nominally formed by ~76.8 vol.% Zr_3Al_2 plus 23.2 vol.% ZrB_2, and were intimately mixed and mechanically activated by HEBM in the form of dry shaker milling for 30 min, next identifying by a dilatometric SPS test at 50 MPa pressure that the densification window of these composites is ~975–1275 °C. Subsequent densification SPS tests at 50 MPa pressure in that temperature interval, and also at 1350 °C, plus the microstructural and mechanical characterisations of the resulting materials, established 1175 °C as the optimal SPS temperature. It was also identified that densification takes place by transient liquid-phase sintering with molten Al, and that it occurs gradually, not abruptly, because most molten Al disappears in a flash by reacting with Zr to form in situ the intermetallic. It is also shown that the combination of HEBM plus reactive SPS yields Zr_3Al_2+ZrB_2 composites with fine-grained microstructures formed essentially by multitudinous ZrB_2 nanograins dispersed within a matrix of sub-micrometre, or nearly submicrometre, Zr_3Al_2 grains. Importantly, these intermetallic–ceramic composites were found to be very hard (i.e., ~11.5 GPa), attributable to the hardening provided by the ZrB_2 nanograins, and fairly tough (i.e., ~4.5 MPa·m$^{1/2}$), and therefore potential candidate materials for a multitude of structural–tribological applications. Finally, implications for future study are discussed.

1. Introduction

Intermetallics based on a transition metal plus Al constitute a broad family of appealing structural materials. This is doubtless the case of the Zr−Al intermetallics, whose interesting combination of physico-chemical properties, including for example low thermal neutron absorption cross-section, high corrosion resistance, adequate biocompatibility, low density, low thermal expansion coefficient, and high refractoriness [1−9], to list some, makes them candidate materials for technological applications in the aerospace, automotive, medical, and nuclear fields, to name but a few.

Notwithstanding the above, Zr−Al intermetallics have still received little attention and remain relatively unexplored, most likely attributable to their compositional−structural complexity and currently difficult processability. Certainly, the binary Zr−Al system is quite complex [10], exhibiting ten possible intermetallic compounds, namely, $ZrAl_3$, $ZrAl_2$, Zr_2Al_3, $ZrAl$, Zr_5Al_4, Zr_4Al_3, Zr_3Al_2, Zr_5Al_3, Zr_2Al, and Zr_3Al, which are essentially line compounds (i.e., each one existing in an extremely narrow concentration range) and have different crystal structures (i.e., cubic, hexagonal, tetragonal, and orthorhombic). Importantly, this great compositional and crystallographic diversity invariably translates into the Zr−Al intermetallics having highly varied mechanical behaviours [1]. Thus for example, there are large differences in hardness between them, ranging from the expected ~18.5 GPa of the hardest $ZrAl_2$ to the ~4.5 GPa of the softest Zr_5Al_4 [1]. Also, according to their bulk modulus to shear modulus ratio, four of them (i.e., Zr_5Al_4, Zr_3Al_2, Zr_5Al_3, and Zr_2Al) are classifiable as ductile [1], and the rest as brittle [1]. Therefore, compositional control is critical to tailor the performance of the Zr−Al intermetallics to the particular needs of a given structural application. As for their processability, Zr−Al intermetallics are as of today preferably fabricated by vacuum arc-melting of ingots [5], repeatedly to ensure homogeneity, which is tedious, time-consuming, costly, and not exempt of other disadvantages (i.e., segregation, contamination from the casting moulds, etc.).

Alternatively, in principle the Zr−Al intermetallics would, like many other intermetallics, be amenable to fabrication by powder metallurgy, which is intrinsically simple, industrially scalable, and cost-effective [11]. Moreover, powder metallurgy (i) allows for near-net-shape manufacture, thus reducing the waste production and minimizing the need for subsequent machining operations, (ii) uses much lower temperatures because the sintering temperatures are typically 0.5−0.8 times the melting temperatures, (iii) provides greater compositional versatility and microstructural control, and (iv) enables innovative multi-particulate designs with ceramics or other dissimilar metals/alloys for tailoring the properties to demand [11]. Despite all this, powder metallurgy has surprisingly yet to be used to fabricate Zr−Al intermetallics or composites based on them, which motivated the present work aimed at demonstrating, for the first time to the best of the authors' knowledge, its potential by fabricating controllably, by means of dry high-energy ball-milling (HEBM) and reactive spark-plasma sintering (SPS), ZrB_2−hardened Zr_3Al_2 intermetallics. Specifically, these particular intermetallic−ceramic composites were chosen as a first demonstration model because (i) Zr_3Al_2 is a ductile but relatively soft (~5.6 GPa) Zr−Al intermetallic [1], which therefore requires second-phase hardening for use in structural applications, and is thus an ideal test-bench within the scope of the present proof-of-concept study, and (ii) ZrB_2 is a very hard, ultra-refractory ceramic [12] that, like Zr_3Al_2, is also based on Zr, so the expectation is that both should be chemically compatible and reactively co-sinterable from Zr, Al, and B powders conveniently subjected to beneficiation. Also, Zr_3Al_2 is an unusual intermetallic that has rarely been observed in the pure state but rather as precipitates during the crystallization of complex amorphous Zr−Al glasses, so that obtaining bulk materials based on it is especially challenging. Moreover, its fabrication by dry HEBM plus reactive SPS, instead of by the typical non-aqueous wet homogenization plus reactive pressureless sintering or reactive hot-pressing, makes processing (i) simpler, because the powder preparation involves a lesser number of steps, (ii) more energy-efficient, because the sintering cycle is ultrafast and consumes less power, and (iii) more environmentally friendly, because the carbon footprint is lower. In what follows, the details of the experimental procedure and the major findings will be described.

2. Experimental procedure

Powders of crystalline ZrH_2 (99.7% purity), crystalline Al (99.8% purity), and amorphous B (95% purity) were purchased commercially (MaTecK, Germany), and combined in the molar ratio of $2ZrH_2$:1Al:1B with the intention of producing an intermetallic−ceramic composite nominally formed by ~76.8 vol.% Zr_3Al_2 and 23.2 vol.% ZrB_2 via the overall reaction $4ZrH_2+2Al+2B\rightarrow Zr_3Al_2+ZrB_2+4H_2(g)$. Brittle ZrH_2 was used instead of ductile Zr for two reasons, namely, (i) it is easier to mill and, because it is the major compound in the powder mixture, it will help to refine the Al and B particles by ductile-brittle and brittle−brittle mechanical alloying thus resulting in a more homogeneous powder mixture [13], and (ii) the $H_2(g)$ resulting from the eventual decomposition of ZrH_2 during SPS can contribute to partially reducing the oxide passivating layers. The combination of powders was next subjected to dry HEBM for 30 min in a shaker mill (Spex D8000, Spex CertiPrep, USA) using hardened steel containers with WC balls (6.7 mm in diameter) under a ball-to-powder weight ratio of 4, in an inert atmosphere of ultrahigh-purity Ar. The inert atmosphere avoids the oxidation of the powder mixture during milling, and was achieved by performing the loading of the balls and powders into the containers, and the container sealing, in a glovebox (CaptairPyramid, Erlab, UK) filled with ultrahigh purity Ar and purged twice. Also, to avoid contamination of the powder mixture during milling, a first sacrificial milling was carried out as described above to thus cover the container and the balls with a thin surface film of the powder mixture, and the resulting milled powder mixture was discarded away. Next, milling was repeated utilizing the same container and balls, using these milled powder mixtures for the rest of the study. This procedure has already been successfully used to mill other powders and powder mixtures without, or with hardly any, contamination by the milling tools [14−18].

The as-milled powder mixtures were then loaded, again within the glovebox filled with ultrahigh purity Ar to minimize their exposure to air, into graphite dies (of 2-cm diameter) lined with graphite foils and covered by graphite blankets, and were consolidated by SPS (HP-D-10, FCT Systeme GmbH, Germany) in dynamic vacuum at various target temperatures (as measured by an axial pyrometer and reached at 100 °C/min), identified by first using the SPS furnace as a dilatometer, for 5 min under 50 MPa pressure (applied at 300 °C). The resulting materials were ground and diamond-polished to a 1-µm finish using conventional procedures, and were characterised (i) microstructurally by water immersion porosimetry (i.e., the Archimedes method), X-ray diffractometry (XRD; D8 Advance, Bruker AXS, Germany), and scanning electron microscopy (SEM; Hitachi S-3600N, Japan or FEI Teneo, FEI Inc., USA) together with energy-dispersive X-ray spectroscopy (EDS; Xflash Detector 3001, Röntec GmbH, Germany or AMETEK, Inc., USA), as well as (ii) mechanically by Vickers indentation tests (Duramin, Struers A/S, Denmark).

3. Results and discussion

Fig. 1 shows the shrinkage-rate curve as a function of temperature logged during a first dilatometric SPS test up to 1600 °C under 50 MPa pressure, performed to determine the optimal range of target temperatures for the subsequent densification SPS tests. It can be seen that the curve is formed
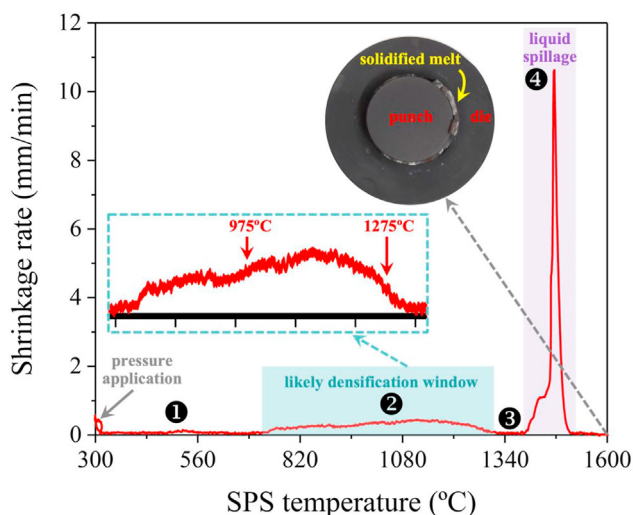

Fig. 1 − **Shrinkage-rate curve as a function of temperature from 300 °C up to 1600 °C logged during the dilatometric SPS test at 50 MPa pressure for the as-milled powder mixture. The onset SPS temperature of 300 °C is because from there onwards heating was performed under pyrometer control. The numbers denote the different stretches identified according to the magnitude of the shrinkage rate. The inset shows the likely densification window in greater detail. Also included is an optical photograph of both the graphite die and punches at the conclusion of the dilatometric SPS test demonstrating the severe liquid spillage occurring at high temperatures.**
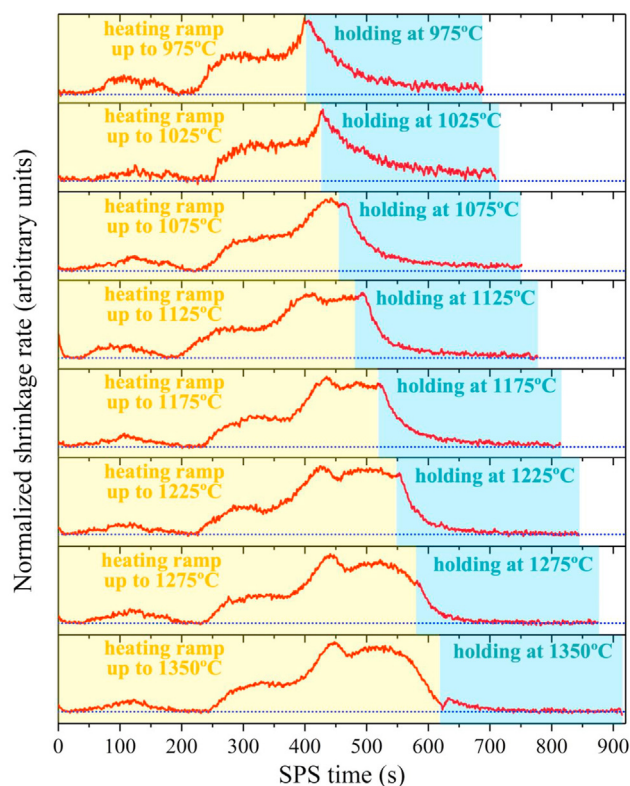

Fig. 2 − **Shrinkage-rate curve as a function of time, normalized to maximum shrinkage rate, logged during the different densification SPS tests, as indicated, at 50 MPa pressure for the as-milled powder mixture. The stages of non-isothermal heating (i.e., 100 °C/min heating ramp up to the desired target temperature) and of isothermal heating (i.e., holding at the desired target temperature for 5 min) are distinguished. The dotted lines are the null shrinkage rate. The SPS time count started from the application of the 50 MPa pressure at 300 °C.**

by four stretches, namely, (i) a first stretch of null shrinkage rate up to ~685 °C with a subtle shrinkage-rate hump centred at ~525 °C, (ii) a second stretch of non-null shrinkage rate from ~685 °C up to ~1300 °C, (iii) a third stretch again of null shrinkage rate from ~1300 °C up to ~1400 °C, and (iv) a fourth stretch of sudden spike and fall of shrinkage rate, centred at ~1465 °C, followed by null shrinkage rate thereafter. It is clear that stretches (i), (iii), and (iv) are impractical in terms of densification, the first because the null shrinkage rate indicates that there is no densification at these low temperatures, the third because the drop of shrinkage rate to zero indicates that full densification had already been achieved during stretch (ii), so that in stretch (iii) only microstructural coarsening will occur, if any at all, and the fourth because the abrupt spike and fall of shrinkage rate came accompanied by direct contact between the two graphite punches, indicating the occurrence of total mass loss by massive liquid spillage. The mere visual observation of the die at the conclusion of the dilatometric SPS cycle, a photograph of which is also included in Fig. 1, confirmed this undesirable scenario. This finding is not a surprise because the expected Zr_3Al_2 is stable up to the peritectic temperature of ~1480 °C where it forms
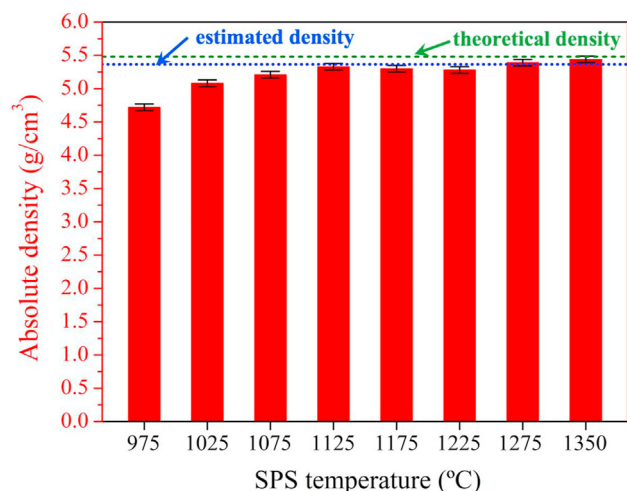
Fig. 3 − Absolute density, as measured by the Archimedes method, of the materials SPS-ed at target temperatures in the range 975−1350 °C for 5 min under 50 MPa pressure. The dashed line is the theoretical absolute density calculated by the rule of mixtures for ~76.8 vol.% Zr$_3$Al$_2$ plus 23.2 vol.% ZrB$_2$. The dotted line is absolute density corrected for the presence of very minor phases.

liquid + Zr$_5$Al$_4$ [10], with Zr$_5$Al$_4$ in turn melting congruently at ~1550 °C [10]. Due to the 50 MPa pressure applied during SPS, the abundant formation of liquid accompanying the peritectic decomposition of Zr$_3$Al$_2$ already caused the complete material spillage out of the die. In any case, this dilatometric SPS test is very instructive because it indicates that the densification window of these materials is ~685−1300 °C, and more likely ~975−1275 °C because the shrinkage rates are higher there, reason for which the subsequent SPS densification tests will be performed at target temperatures within that latter interval. Nonetheless, SPS at 1350 °C will also be carried out to elucidate if this results in enhanced hardness and/or fracture toughness. Importantly, an earlier study on SPS of ZrB$_2$−ZrH$_2$ has shown that ZrH$_2$ decomposes to Zr + H$_2$(g) before 600 °C [19], so the release of H$_2$(g) will not hinder the densification of the present composites because the high interconnected and open porosity existing at that initial sintering stage will allow the H$_2$(g) generated to leave the powder compact without becoming trapped and occluded in the microstructure.

Fig. 2 the shrinkage-rate curves as a function of time logged during the subsequent densification SPS tests at target temperatures in the range 975−1350 °C for 5 min under 50 MPa pressure. It can be seen that there is always a first weak shrinkage-rate peak centred at ~120−150 s, corresponding to ~500−550 °C, attributable to the mass loss accompanying the decomposition of ZrH$_2$ into Zr + H$_2$(g) [19]. More importantly, it can be seen that, after increasing appreciably, eventually the shrinkage rate faded for the SPS tests performed at 1125−1175 °C or higher temperature, indicating complete densification, but not for the SPS tests performed in the temperature range 975−1075 °C, indicating incomplete densification. Therefore, according to the shrinkage-rate curves, 1125−1175 °C is the optimal SPS temperature (although impossible now, subsequent results will allow discrimination

between these two temperatures). However, it is likely that much longer SPS cycles at lower temperatures could also result in complete densification, but given the high heating rates used in SPS and that diffusion increases exponentially with temperature and linearly with time, it is much more recommendable to slightly increase the target SPS temperature up to the optimal than to hold for a long time at lower temperatures.

Fig. 3 shows the values of absolute density of the materials SPS-ed at 975−1350 °C for 5 min under 50 MPa pressure, as measured by the Archimedes method, confirming that 1125−1175 °C is the optimal SPS temperature. Certainly, it can be seen that the materials SPS-ed at 975−1075 °C have lower absolute density than those SPS-ed at higher temperatures, indicating that the former are porous (more so the lower their SPS temperature) if the latter are dense. They all have an absolute density lower than that calculated for ~76.8 vol.% Zr$_3$Al$_2$ plus 23.2 vol.% ZrB$_2$, but those SPS-ed at and above 1125 °C have the density expected considering the presence of small relative proportions (i.e., ~3−5 vol.%) of other phases as will be shown later by XRD and SEM/EDS.

The analysis of the shrinkage-rate curves in Fig. 2 also indicates that densification began at 224 ± 15 s, equivalent to ~673 ± 25 °C which is, within the errors, the Al melting point (i.e., ~660.3 °C). It also indicates that there was no densification burst at that temperature, but rather that complete densification was achieved gradually and at much higher temperatures (i.e., at ~1125−1175 °C according to Fig. 3, which is almost twice the Al melting point). Therefore, it follows that reactive SPS initiated at the Al melting point, which was the logical expectation because molten Al is the first liquid to be formed since Zr and B melting points are much higher (i.e., ~1855 °C and 2076 °C, respectively) and there are no eutectic temperatures below the Al melting point. Moreover, it is foreseeable that there would have been little or no solid-state densification by Zr−Al interdiffusion prior to the formation of molten Al because the heating ramp applied during SPS was ultrafast (i.e., 100 °C/min). It can thus be inferred that the formation of molten Al favoured densification, but that there was no sudden densification because much of the molten Al would have been consumed in a flash by immediately reacting with Zr. This ultrafast reaction kinetics would be ascribable to the mechanical activation induced by HEBM (i.e., intimate mixing of the reactants, small crystal sizes, abundant structural defects, and large specific surface areas). Whichever the case, densification of these materials occurred by transient (almost "fugitive") liquid-phase sintering [20].

Fig. 4 shows the XRD patterns of the materials SPS-ed at 975−1350 °C for 5 min under 50 MPa pressure, and the Pawley refinement performed for one of them. It can be seen in Fig. 4A that, as expected, they all are composed of tetragonal Zr$_3$Al$_2$ (P4$_2$/mnm) as major phase and hexagonal ZrB$_2$ (P6/mmm) as minor phase, plus monoclinic ZrO$_2$ (P2$_1$/c), tetragonal ZrO$_2$ (P4$_2$/nmc), cubic Al and MgO (F $\overline{m}$ 3m), and orthorhombic Zr$_2$Al$_3$ (Fdd2) in very low, or even trace, relative abundances. By way of example it can be seen in Fig. 4B for the material SPS-ed at 1175 °C that the corresponding Pawley refinements captured the experimental XRD patterns very well (i.e., χ_r^2 <1.35), thus confirming the correctness of the aforementioned phase in-
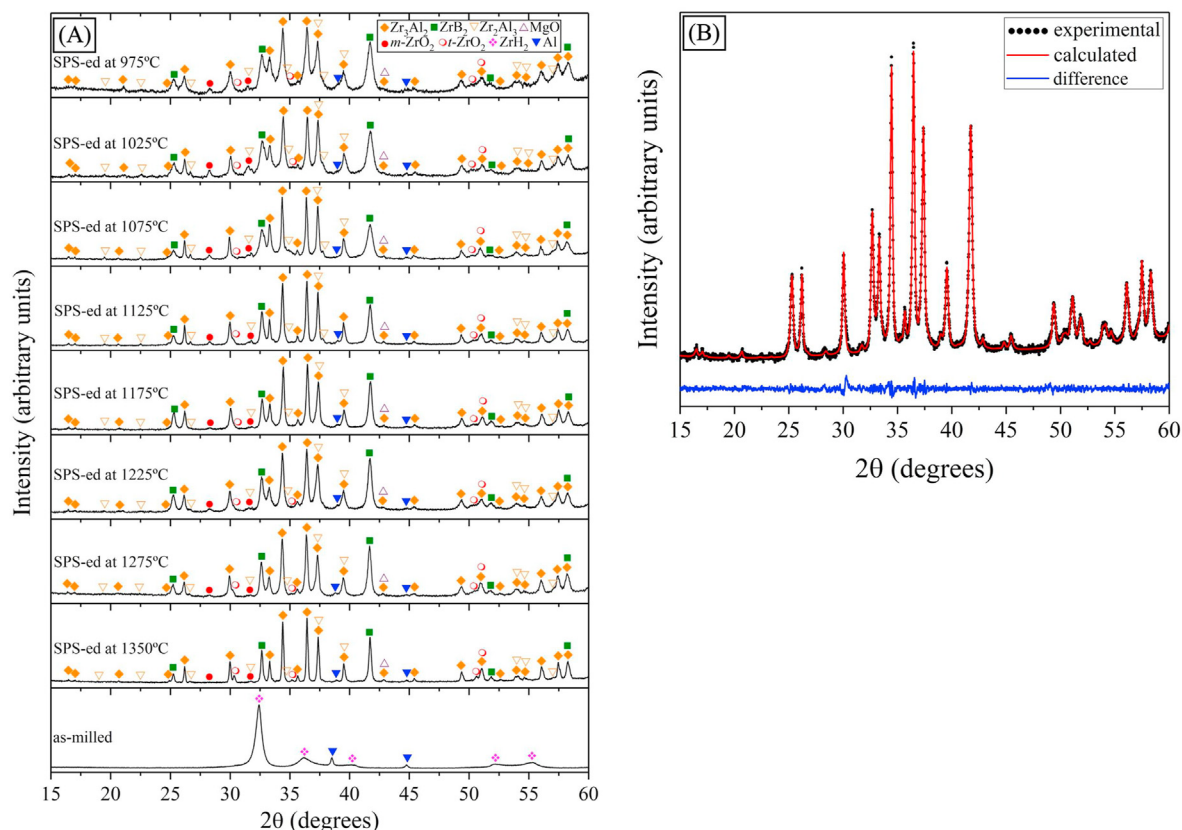
Fig. 4 – (A) XRD patterns (15–60° 2θ) of the materials SPS-ed at target temperatures in the range 975–1350 °C for 5 min under 50 MPa pressure and of the as-milled powder mixture, as indicated. Peak assignations are included. The XRD patterns were all acquired with CuKα incident radiation and were indexed using the PDF2 database. The letters *m* and *t* mean monoclinic and tetragonal, respectively. **(B)** Pawley refinement, performed with Topas 4.2 (Bruker AXS, Germany), of the XRD pattern of the material SPS-ed at 1175 °C for 5 min under 50 MPa pressure.

ventory. Interestingly, it can also be seen in Fig. 4A that the XRD peaks of Zr_3Al_2 and ZrB_2 become increasing narrow with increasing SPS temperature, and especially at 1350 °C, indicating the corresponding growth of the Zr_3Al_2 and ZrB_2 crystallites. This is the logical expectation considering that the diffusion coefficients increase exponentially with temperature. Importantly, according to its XRD pattern, also included in Fig. 4A as a referent for comparison, the as-milled powder mixture only contains crystalline ZrH_2 and Al, plus B that, because it is amorphous, gives no XRD peaks. This rules out that Zr_3Al_2 and ZrB_2 were formed during HEBM. It can also be seen that (i) there are no WC peaks either, confirming the desired absence of contamination by the milling tools thanks to the first sacrificial milling, and (ii) that the ZrH_2 peaks are much broader than the Al peaks, reflecting the also expected much greater comminution of the ZrH_2 particles owing to its brittle nature. Indeed, using the Scherrer method [21], the crystallite sizes of ZrH_2 and Al are roughly estimated to be ~80 nm and 0.4 μm, respectively. Therefore, the importance of the XRD patterns in Fig. 4A is that they (i) evince the mechanical activation of the powder mixture during HEBM and (ii) confirm the occurrence *in situ* during SPS of the reaction $4ZrH_2+2Al+2B \rightarrow Zr_3Al_2+ZrB_2+4H_2(g)$ (*i.e.*, first $ZrH_2(s) \rightarrow Zr(s)+2H_2(g)$ at ~500–550 °C and then $4Zr(s)+2Al(l)+2B(s) \rightarrow$

$Zr_3Al_2(s)+ZrB_2(s)$ at ~660 °C and above), thus demonstrating that the powder-metallurgy fabrication route used here, based on HEBM plus reactive SPS, enables the compositional design and controlled fabrication of Zr–Al intermetallics and of composites based on them with ceramic reinforcements. Note that the presence of some ZrO_2 in the SPS-ed materials is not a surprise despite the milling and powder loading into the dies having been performed under Ar atmosphere because spontaneous passivation is expected to occur during placement of the dies in the chamber of the SPS furnace, it being impossible to completely reduce the passivating layers by the $H_2(g)$ released at ~500–550 °C. Earlier studies on other composites have shown that the oxides crystallize from these passivating layers during SPS [22]. The presence of ZrO_2, which is unavoidable unless an SPS furnace with integrated glovebox is used (a type that is already commercially available for medium-scale production), is not detrimental because it is much harder (*i.e.*, ~16 GPa) than Zr_3Al_2. The presence of MgO is not a surprise either because Mg is a typical impurity in B powders, which are often synthesized by magnesiothermic reduction of B_2O_3 or H_3BO_3, and Mg is very prone to passivation. The presence of MgO would be avoidable, or at least minimizable, by using higher-purity B powders. ZrO_2 and MgO were, however, not detected by XRD in the as-milled powder
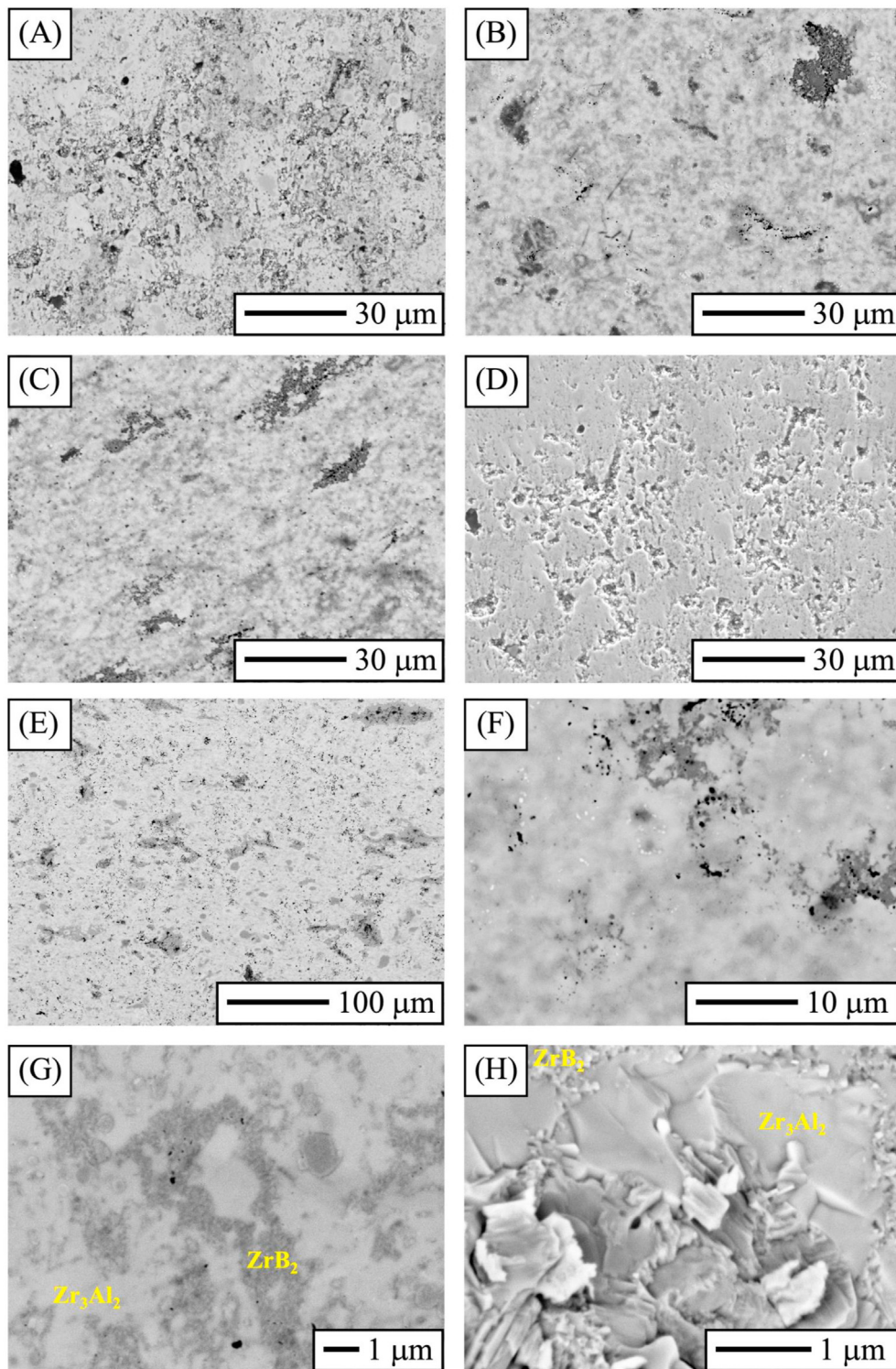
Fig. 5 — SEM micrographs representative of the microstructure of the materials SPS-ed at target temperatures in the range 975—1350 °C for 5 min under 50 MPa pressure. (A)—(C) are images of the polished surface of the materials SPS-ed at 950 °C, 1175 °C, and 1350 °C, respectively, taken using backscattered electrons, and (D) is the same image as (A) but taken with secondary electrons. (E)—(F) are images of the polished surface of the material SPS-ed at 1225 °C taken at low and high magnifications, respectively, with backscattered electrons. (G)—(H) are images of the fracture surface of the material SPS-ed at 1275 °C taken at much higher magnifications with backscattered electrons. Imaging was done at 15 keV.
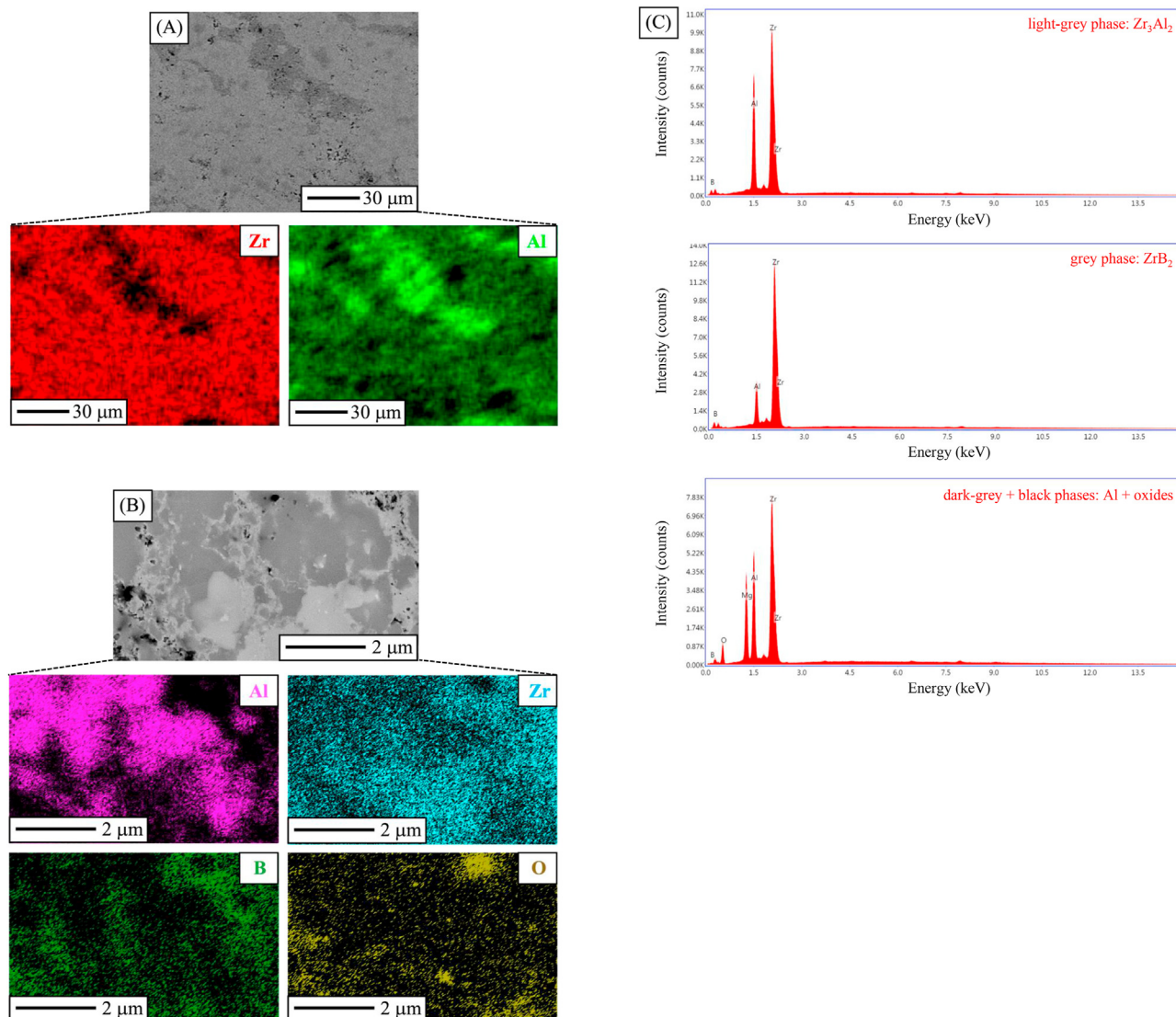
Fig. 6 — Representative EDS analyses performed selectively on some of the materials fabricated. (A) Low-magnification SEM micrograph and corresponding elemental composition maps of Zr and Al acquired on the material SPS-ed at 1225 °C. (B) High-magnification SEM micrograph and corresponding elemental composition maps of Al, Zr, B, and O acquired within the typical dark-grey regions in Fig. 5A—C on the material SPS-ed at 1275 °C. (C) Point EDS spectra acquired on the material SPS-ed at 1275 °C at selected locations, as indicated. The SEM images in (A) and (B) were taken with backscattered electrons. Imaging and EDS analysis were done at 15 keV.

mixture because these and other oxide passivating layers are amorphous and very thin [23]. Zr_2Al_3 is present in trace proportions, and, in any case, is not detrimental either because it is also theoretically much harder (i.e., ~12.5 GPa) than Zr_3Al_2.

By way of example, Fig. 5 shows a set of SEM images representative of the microstructure of the materials SPS-ed at 975–1350 °C for 5 min under 50 MPa pressure, and Fig. 6 the EDS analyses performed on some of them. The comparison of Fig. 5A—C evinces the differences of densification achieved by SPS at target temperatures lower than, equal to, or higher than 1175 °C. Certainly, it can be seen in Fig. 5A, and more clearly in Fig. 5D, that the material SPS-ed at 975 °C is very porous, which, although to a lesser extent, was also the case for those SPS-ed at 1025 °C and 1075 °C, and in Fig. 5B and C that on the contrary the materials SPS-ed between 1175 °C

and 1350 °C are all fully dense. Hence, the SEM observations corroborate the conclusions of densification already drawn from the shrinkage-rate curves in Fig. 2 and from the absolute density measurements in Fig. 3. It can also be seen in Fig. 5A—C that the microstructures exhibit evident compositional contrasts (i.e., light grey, grey, dark grey, and black), which is additional evidence for the multi-phase nature of these materials. Considering the phase inventory determined from the XRD patterns in Fig. 4A, the low- and high-magnification EDS maps in Fig. 6A and B, and the point EDS spectra in Fig. 6C, the light-grey phase is assignable to Zr_3Al_2 and very occasionally to Zr_2Al_3, the grey phase to ZrB_2 and occasionally to ZrO_2, the dark-grey phase to Al, and the black phase to MgO. Lower- and higher-magnification SEM images, such as those shown by way of example in Fig. 5E and F for the
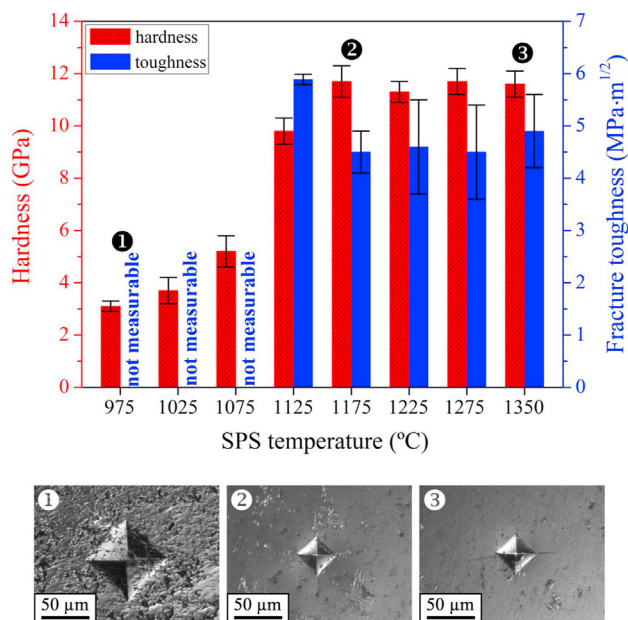
Fig. 7 − Hardness and fracture toughness of the materials SPS-ed at target temperatures in the range 975−1350 °C for 5 min under 50 MPa pressure, as measured by Vickers indentation tests at 9.8 N load. Fracture toughness was calculated considering Palmqvist-type cracks. For visual reference purposes, optimal micrographs are presented of the Vickers indents for the materials SPS-ed at 975 °C (❶), 1175 °C (❷), and 1350 °C (❸).

material SPS-ed at 1225 °C, revealed that Zr_3Al_2 is, as expected, the main phase and that it constitutes a matrix embedding the other phases. The former is consistent with the relative abundance of the reaction products expected according to the molar formulation of the powder mixture, and the latter with a densification occurring by transient liquid-phase sintering with molten Al and attendant formation of Zr_3Al_2. ZrB_2 is the second most abundant phase, and is homogeneously distributed throughout the entire microstructure. Some Al is accumulated in minority, randomly dispersed, regions which, according to the SEM image and EDS maps in Fig. 6B, also contain ZrB_2 grains and tiny MgO grains. The existence of some ZrO_2 and B_2O_3 in these regions cannot be excluded. Because during HEBM Al was intimately mixed with ZrH_2 and B, and was refined sufficiently, it is unlikely that these regions of Al + ZrB_2+oxides are due to the formation of Al pools. Hence, it is reasonable to think that they most likely formed in the vicinity of regions locally richer in ZrO_2, with the excess Al being the result of the remaining Zr reacting with B to form ZrB_2 instead of an intermetallic richer in Al than Zr_3Al_2. The EDS maps in Fig. 6A are consistent with this hypothesis. Interestingly, higher-magnification SEM images of the fracture surfaces, such as those shown by way of example in Fig. 5G and H for the material SPS-ed at 1275 °C, revealed the true microstructural scale of these materials, showing that they have fine-grained microstructures, but according to the XRD patterns in Fig. 4A less so with increasing SPS temperature, formed essentially by multitudinous ZrB_2 nanograins embedded in a matrix of submicrometre, or nearly

submicrometre, Zr_3Al_2 grains (confirmed by point EDS analyses). This size difference is because the former were formed by the solid-state reaction between Zr and B nanograins and during the cycles of SPS at 975−1350 °C they underwent low homologous temperatures, of only ~0.30−0.42, because the ZrB_2 melting point is ~3246 °C [12], and the latter were formed by the solid−liquid reaction between Zr nanograins and molten Al and underwent much higher homologous temperatures, of 0.66−0.91, because Zr_3Al_2 decomposes peritectically at ~1480 °C [10].

Fig. 7 shows the values of hardness and fracture toughness determined by Vickers indentation tests for the materials SPS-ed at 975−1350 °C for 5 min under 50 MPa pressure. It can be seen that those SPS-ed at 975−1025 °C are soft (i.e., <5.5 GPa), that the one SPS-ed at 1125 °C is moderately hard (i.e., ~10 GPa), and that those SPS-ed at 1175−1350 °C are all very hard (i.e., ~11.5 GPa) and, within the errors, equally so. By way of example, Fig. 7 also includes optical micrographs of some residual imprints, where it can be seen that the size differences speak for themselves. Moreover, these optical micrographs also show that the materials SPS-ed at 1175 °C or above are also much more wear resistant because they were comparatively much less susceptible to chipping during diamond polishing. Interestingly, because mechanical properties are strongly affected by slight densification differences, hardness measurements break the hitherto ambiguity between 1125 °C and 1175 °C, discriminating 1175 °C as being the optimal SPS temperature. Lower SPS temperatures yield increasingly porous, and therefore softer, materials, and higher SPS temperatures are impractical because, all materials being already fully dense and not having large microstructural differences, hardness no longer increases. Importantly, ~11.5 GPa is twice the ~5.5 GPa theoretical hardness of Zr_3Al_2 [1], evincing the hardening provided by ZrB_2 (whose hardness is greater than 20 GPa [12]). The hardness of these intermetallic−ceramic composites, which is much greater than that of many typical structural metals and alloys and even similar to that of some structural ceramics and cermets fabricated at higher temperature (such as cordierite [24], mullite [25], and medium-grained WC-15Co [26], to name a few examples), classifies them as hard materials (i.e., >10 GPa hardness). It can also be seen in Fig. 7 that the ~11.5 GPa hardness comes accompanied by a fracture toughness of ~4.5 MPa·$m^{1/2}$. Note that the ~5.9 MPa·$m^{1/2}$ toughness of the material SPS-ed at 1125 °C is artificially overestimated due to its slight residual porosity, and that the materials SPS-ed at 975−1075 °C are so porous that they did not even generate radial cracks during Vickers testing, so ~4.5 MPa·$m^{1/2}$ is indeed the true indentation fracture toughness of these materials. This toughness, although only moderate because intermetallics have an intrinsic toughness intermediate between metals and ceramics and because these composites have fine-grained microstructures, is nonetheless enough for many structural applications. Toughness could be increased via microstructural coarsening, achievable by much longer SPS cycles at the higher temperatures or post-SPS annealing, but unfortunately this would likely degrade other mechanical properties (such as strength and wear resistance), so there will always be a price to pay depending on the microstructural scale.

To close, it is worthwhile highlighting the virtues of the present powder-metallurgy fabrication route, and giving an

outline of future research directions. First, HEBM is key because it provides the powder mixture with the desired features, namely, (i) the homogeneous dispersion and inter-mixing of the elemental constituents that avoid the formation of isolated liquid pools, and (ii) the mechanical activation of the powder mixture that favours the reactive sintering and getting fine-grained microstructures. With this in mind, future work should investigate the influence of the degree of mechanical activation, as dictated by the HEBM variables (*i.e.*, milling time and powder charge), on the densifiability, microstructure, and properties of these materials. And second, SPS is also key because it provides the desired densification cycle for the compact powder, namely, (i) the ultrafast heating that minimizes the undesirable solid-state Zr−Al interdiffusion that consumes Al useful for densification, (ii) the high uniaxial pressure that provides an additional driving force for densification, and (iii) the more than likely enhanced sinterability assisted by the electric field. With this in mind, future work should also investigate the influence of the SPS variables other than temperature (*i.e.*, pressure, heating rate, holding time, pulsed current, *etc.*) on the densifiability, microstructure, and properties of these materials. Moreover, the powder-metallurgy fabrication route used here seems very generic and tantalizingly applicable to the development of a great diversity of intermetallics and intermetallic−ceramic composites, and therefore exploration of this potential also deserves future research effort. Finally, it is also advocated the need to extend these studies towards the near-net shape manufacture of intermetallics and of intermetallic−ceramic composites with complex geometries, by combining HEBM with wet or plastic shaping of green parts and their pressureless sintering (both conventional and especially ultrafast).

4.   Conclusions

A proof-of-concept study was conducted of the fabrication by powder metallurgy, using HEBM and reactive SPS, of ZrB_2-−hardened Zr_3Al_2 intermetallic model composites. Based on the experimental results and analyses, the following conclusion can be drawn:

1. HEBM of ZrH_2, Al, and B powders combined in molar ratios 2:1:1 yields a mechanically-activated powder mixture featuring an intimate mixture of very refined particles.
2. Reactive SPS of the as-milled $2ZrH_2+Al + B$ powder mixture occurs by transient liquid-phase sintering with molten Al, despite which the densification is gradual, not abrupt, because most of the molten Al reacts in a flash with Zr to form *in situ* the intermetallic.
3. The so-fabricated intermetallic−ceramic composites have the desired composition and fine-grained microstructures formed essentially by multitudinous ZrB_2 nanograins dispersed in a matrix of submicrometre, or nearly sub-micrometre, Zr_3Al_2 grains.
4. The present reactive SPS is optimal at 1175 °C, at which temperature dense ZrB_2−hardened Zr_3Al_2 intermetallic composites with a high hardness of ~11.5 GPa and a

sufficient fracture toughness of ~4.5 $MPa·m^{1/2}$ are already obtained.
5. HEBM plus reactive SPS is a combination that potentially is suitable to fabricate controllably, by powder metallurgy, a great diversity of intermetallics and intermetallic−ceramic composites for structural applications, and therefore it merits exploration and exploitation.

Declaration of Competing Interest

The authors declare that they have no known competing financial interests or personal relationships that could have appeared to influence the work reported in this paper.

Acknowledgements

REFERENCES

[1] Duan YH, Huang B, Sun Y, Peng MJ, Zhou SG. Stability, elastic properties and electronic structures of the stable Zr−Al intermetallic compounds: a first-principles investigation. J Alloys Compd 2014;590:50−60.

[2] Laik A, Bhanumurthy K, Kale GB. Intermetallics in the Zr−Al diffusion zone. Intermetallics 2004;12(1):69−74.

[3] Schulson EM. In: Westbrook JH, Fleischer RL, editors. Intermetallic compounds, vol. 2. New York: John Wiley & Sons; 1994.

[4] He W, Chen X, Liu N, Luan B, Yuan G, Liu Q. Cryo-rolling enhanced inhomogeneous deformation and recrystallization grain growth of a zirconium alloy. J Alloys Compd 2017;699:160−9.

[5] Zhang X, Zhang B, Liu SG, Xia CQ, Zhang XY, Ma MZ, et al. Microstructures and mechanical properties of Zr−Al binary alloys processed by hot-rolling. Mater Sci Eng A 2020;773:138723.

[6] Kutty TRG, Ravi K, Ganguly C. Studies on hot hardness of Zr and its alloys for nuclear reactors. J Nucl Mater 1999;265(1):91−9.

[7] He W, Chen X, Liu N, Luan B, Yuan G, Liu Q. Cryo-rolling enhanced inhomogeneous deformation and recrystallization grain growth of a zirconium alloy. J Alloys Compd 2017;699:160−9.

[8] Kondo R, Nomura N, Suyalatu, Tsutsumi Y, Doi H, Hanawa T. Microstructure and mechanical properties of as-cast Zr−Nb alloys. Acta Biomater 2011;7(12):4278−84.

[9] Russell RB. Coefficients of thermal expansion for zirconium. JOM 1954;6(9):1045−52.

[10] Murray J, Peruzzi A, Abriata JP. The Al−Zr (aluminum−zirconium) system. J Phase Equil 1992;13(2):277−91.

[11] Esteban PG, Bolzoni L, Ruiz-Navas EM, Gordo E. PM processing and characterization of Ti−7Fe low cost titanium alloys. Powder Metall 2011;54(3):242−52.

[12] Guo S-Q. Densification of ZrB_2—based composites and their mechanical and physical properties: a review. J Eur Ceram Soc 2009;29(6):995—1011.

[13] Suryanarayana C. Mechanical alloying and milling. Prog Mater Sci 2001;46(1—2):1—184.

[14] Zamora V, Ortiz AL, Guiberteau F, Nygren M, Shaw LL. On the crystallite size refinement of ZrB_2 by high-energy ball-milling in the presence of SiC. J Eur Ceram Soc 2011;31(13):2407—14.

[15] Zamora V, Ortiz AL, Guiberteau F, Nygren M. On the enhancement of the spark-plasma sintering kinetics of ZrB_2—SiC powder mixtures subjected to high-energy co-ball-milling. Ceram Int 2013;39(4):4191—204.

[16] Núñez-González B, Ortiz AL, Guiberteau F, Nygren M. Spark-plasma-sintering kinetics of ZrC—SiC powder mixtures subjected to high-energy co-ball-milling. Ceram Int 2013;39(8):9691—7.

[17] Zamora V, Guiberteau F, Ortiz AL. Effect of high-energy ball-milling on the spark plasma sinterability of ZrB_2 with transition metal disilicides. J Eur Ceram Soc 2020;40(15):5020—8.

[18] Zamora V, Guiberteau F, Ortiz AL. Fabrication of ultrafine-grained ZrC—Co cemented carbides with superior sliding-wear resistance from micrometre starting powders. Ceram Int 2021;47(17):24831—40.

[19] Ran S, Huang SG, Van der Biest O, Vleugels J. High-strength ZrB_2—based ceramics prepared by reactive pulsed electric current sintering of ZrB_2—ZrH_2 powders. J Eur Ceram Soc 2012;32(10):2537—43.

[20] German RM. Sintering theory and practice. New York: Wiley; 1996.

[21] Ortiz AL, Shaw L. X-ray diffraction analysis of a severely plastically deformed aluminum alloy. Acta Mater 2004;52(8):2185—97.

[22] Zamora V, Ortiz AL, Guiberteau F, Nygren M. In situ formation of ZrB_2—ZrO_2 ultra-high-temperature ceramic composites from high-energy ball-milled ZrB_2 powders. J Alloys Compd 2012;518:38—43.

[23] Ortiz AL, Zamora V, Rodríguez-Rojas F. A study of the oxidation of ZrB_2 powders during high-energy ball-milling in air. Ceram Int 2012;38(4):2857—63.

[24] Camerucci MA, Urretavizcaya G, Cavalieri AL. Mechanical behavior of cordierite and cordierite—mullite materials evaluated by indentation techniques. J Eur Ceram Soc 2001;21(9):1195—204.

[25] Anya CC, Hendry A. Sintering, hardness and indentation fracture toughness (KIC) of mullite and its composite with 15 wt% X-phase sialon. J Eur Ceram Soc 1994;13(3):247—56.

[26] García J, Collado Ciprés V, Blomqvist A, Kaplan B. Cemented carbide microstructures: a review. Int J Refract Metals Hard Mater 2019;80:40—68.